ACS APPLIED NANO MATERIALS

Cite This: *ACS Appl. Nano Mater.* 2018, 1, 4283−4293

Article

www.acsanm.org

Development of Co$_3$[Co(CN)$_6$]$_2$/Fe$_3$O$_4$ Bifunctional Nanocomposite for Clinical Sensor Applications

Caio Lenon C. Carvalho,[†] Anna Thaise B. Silva,[†] Roberto A. S. Luz,[†,‡]
Gustavo Montgomery B. Castro,[‡] Cleanio da Luz Lima,[§] Valmor Roberto Mastelaro,[∥]
Robson Rosa da Silva,[∥] Osvaldo N. Oliveira, Jr.,*[∥] and Welter Cantanhêde*[†]

[†]Departamento de Química, Centro de Ciências da Natureza, Universidade Federal do Piauí, Teresina, 64049-550, Piauí, Brazil
[‡]Centro de Ciências da Natureza, Universidade Estadual do Piauí, Teresina, 640002-200, Piauí, Brazil
[§]Departamento de Física, Centro de Ciências da Natureza, Universidade Federal do Piauí, Teresina, 64049-550, Piauí, Brazil
[∥]Instituto de Fisica de São Carlos, Universidade de São Paulo, São Carlos-São Paulo CEP 13560-970, Brazil

Ⓢ *Supporting Information*

ABSTRACT: In this study, a magnetically separable three-dimensional (3D) Co$_3$[Co(CN)$_6$]$_2$/Fe$_3$O$_4$ nanocomposite comprising magnetic nanoparticles (NPs) adsorbed on the nanocubes of a cobalt Prussian blue analogue was prepared. The nanocomposite exhibited enhanced electrochemical performance in Co^{2+}/Co^{3+} conversion, while the super-paramagnetic behavior of the magnetite NPs was preserved even after adsorption on the nanocubes. Increased Faradaic currents were observed in the cyclic voltammograms (CV) for Co$_3$[Co(CN)$_6$]$_2$/Fe$_3$O$_4$ in comparison with the CV of isolated Co$_3$[Co(CN)$_6$]$_2$. This increase was attributed to

supramolecular charge transfer between the cobalt Prussian blue analogue and the magnetic NPs and the larger amount of electroactive species on the electrode. Transmission electron microscopy images showed well-defined Co$_3$[Co(CN)$_6$]$_2$ nanocubes that had edge lengths of 21−140 nm and were decorated with spherical magnetite NPs less than 10 nm in diameter. Interestingly, an intimate contact between the nanocubes and aggregate formation was avoided by Fe$_3$O$_4$ NPs. The composition, morphology, and surface properties of the nanohybrid material were assessed by UV−vis absorption spectroscopy, FTIR spectroscopy, X-ray diffraction, scanning electron microscopy, and Brunauer−Emmett−Teller surface area. The analytical results of nanocomposite showed main bands, crystalline phases, and structures associated with Fe$_3$O$_4$ and Co$_3$[Co(CN)$_6$]$_2$. The bifunctional properties of Co$_3$[Co(CN)$_6$]$_2$/Fe$_3$O$_4$ are potentially useful for building novel (bio)sensors and magnetic devices for clinical applications.

KEYWORDS: nanocomposite, cobalt Prussian blue analogue, magnetite nanoparticles, magnetically separable, performance electrochemical, precipitation method
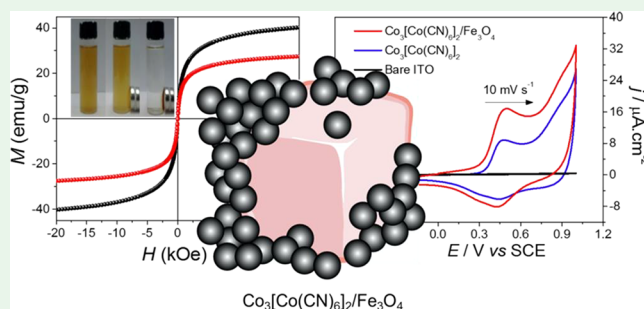
1. INTRODUCTION

Modified nanostructures that have been tailored for specific applications have seen a lot of progress in recent years.[1−5] These are typically supramolecular three-dimensional (3D) structures, where synergy is reached between the components interacting at the molecular level through covalent or reversible noncovalent interactions.[6] They may be built with ferromagnetic materials, metallic nanoparticles,[7,8] quantum dots,[9,10] biomolecules and polymers,[11,12] and hybrid materials. Multi-functionality of these hybrids can be exploited for applications involving magnetic response,[13] electrical,[14] electrochemical,[15] optical,[16] luminescent,[17] and catalytic[18] properties, biological compatibility,[19] and drug-delivery ability.[20] Prussian blue analogues (PBAs) are relevant in this context, because they can be easily synthesized[27−29] and exhibit various desirable properties that have allowed their application in ion exchange for removal of radioactive cesium (Cs), gas storage, and

electrochemical energy storage.[21−27] PBAs can form homo- and heteropolynuclear complexes with the general formula A$_m$[B(CN)$_6$]$_n$, where A and B are transition metal ions.[30] PBAs consisting of cobalt(II) hexacyanoferrate(III) (Co$_3$[Fe(CN)$_6$]$_2$) nanocrystals homogeneously dispersed in polyaniline (PANI) have been used as high-performance catalysts[31,32] for oxygen reduction reaction (ORR). MnO$_x$-FeO$_y$ nanocage catalysts were synthesized via thermal decomposition of Mn$_3$[Fe(CN)$_6$]$_2$·nH$_2$O and used to investigate the size effects of metal oxides in the low-temperature catalytic reduction of NO$_x$ with NH$_3$.[32] In electrochemical energy storage, PBAs have been utilized in electrodes for fabricating supercapacitors and batteries owing to their 3D structure with open spaces that

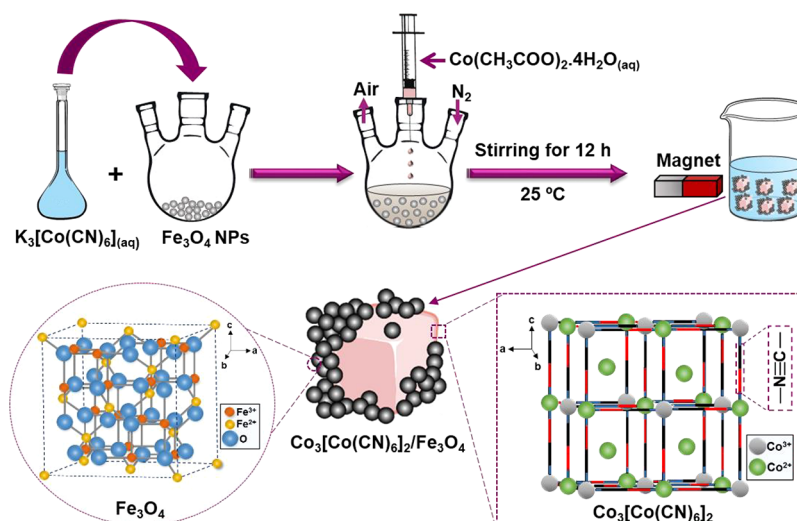**Figure 1.** Schematic representation for the fabrication of $Co_3[Co(CN)_6]_2/Fe_3O_4$.

can accommodate ions and neutral molecules of various sizes, with fast charge and discharge in electrochemical cycling.[33,34]

Cobalt(II) hexacyanocobaltate(III), $Co_3[Co(CN)_6]_2$, is a typical mixed valence homopolynuclear compound with metallic centers linked by cyanide bridges,[21,35] which can be either hydrated or anhydrous. Its structure is not affected by dehydration and there is only a visible change in color from pink $Co_3[Co(CN)_6]_2 \cdot nH_2O$ to blue $Co_3[Co(CN)_6]_2$.[30,36] Zhang and colleagues have investigated the fine-tuning thermochromic properties of $Co_3[Co(CN)_6]_2 \cdot nH_2O$, in which the change in coordination environment of Co^{2+} ions with citrate resulted in a color transition from pink to blue upon heating.[29] A similar effect attributable to alterations in the coordination atmosphere of Co^{2+} ions has been observed for PBA-containing films.[37]

Hybrids made with PBA decorated with nanoparticles may have enhanced properties, as demonstrated by the increased catalytic activity in the coupling reactions of aryl chlorides using $Co_3[Co(CN)_6]_2$ nanocrystals modified with palladium nanoparticles (Pd NPs), $Pd–Co_3[Co(CN)_6]_2$.[38] Following this approach, the structure of $Co_3[Co(CN)_6]_2$ nanocubes was modified by macrocyclic β-cyclodextrin (β-CD) using supramolecular self-assembly, which is a promising host–guest system in the design of (bio)sensors.[39] On the basis of these results, one may envisage the use of magnetite nanoparticles (Fe_3O_4 NPs)[40,41] as a building block to exploit their magnetic response at room temperature.[42−47] Indeed, a magnetic adsorbent containing Fe_3O_4 NPs and Prussian blue nanoparticles (PB NPs) has been shown to be highly efficient in the removal of ^{137}Cs with rapid magnetic separation.[48]

To the best of our knowledge, spectroscopic, structural, and electrochemical studies of $Co_3[Co(CN)_6]_2$ nanocubes decorated with magnetite nanoparticles have not been reported to date. In this work, the strategy of decorating cobalt Prussian blue analogue nanocubes (Co-PBA NCs) with Fe_3O_4 magnetic nanoparticles is an attempt to combine the magnetic and electrochemical properties of the two materials. The morphology, magnetic properties, electrochemical performance, surface properties, and structural organization of the hybrid were a combination of its constituents, as assessed by ultraviolet–visible (UV–vis) and Fourier transform infrared (FTIR) spectroscopy, X-ray diffraction (XRD), transmission

electron microscopy (TEM), vibrating sample magnetometer (VSM), cyclic voltammetry (CV), scanning electron microscopy (SEM), Brunauer−Emmett−Teller (BET) surface area measurements, and X-ray photoelectron spectroscopy (XPS).

2. EXPERIMENTAL SECTION

2.1. Chemicals and Materials. Iron(III) chloride hexahydrate (99%, $FeCl_3 \cdot 6H_2O$) and iron(II) chloride tetrahydrate (99%, $FeCl_2 \cdot 4H_2O$) were purchased from Sigma-Aldrich. Potassium hexacyanocobaltate(III) (95%, $K_3[Co(CN)_6]$) and cobalt(II) acetate tetrahydrate (98%, $Co(CH_3COO)_2 \cdot 4H_2O$) were obtained from Acros Organics. Sodium hydroxide (99%, NaOH) was acquired from Impex. Acetone (99.5%) and sodium chloride (99%) were purchased from Synth and Isofar, respectively. All chemicals were used without further purification and the solutions were prepared with ultrapure water (purified by a Purelab Option-Q (Elga) system, resistivity >18.2 MΩ cm).

2.2. Synthesis of Nanocubes of Cobalt Prussian Blue Analogue ($Co_3[Co(CN)_6]_2$ NCs). $Co_3[Co(CN)_6]_2$ NCs were prepared by slight modifications of the method reported by Carvalho et al.[39] and Hu et al.[49] In a reaction flask, 16.6 mg (5×10^{-5} mol) of $K_3[Co(CN)_6]$ were dissolved in 10 mL of ultrapure water. Next, 10 mL of 7.5 mmol L^{-1} $Co(CH_3COO)_2 \cdot 4H_2O$ (18.7 mg, 7.5×10^{-5} mol) were added slowly to the solution containing Co^{3+} species under a nitrogen flow at 25 °C, yielding a slightly pink colloidal suspension. The reaction mixture was stirred for 12 h, after which the product was washed three times with acetone to eliminate any unreacted starting materials. After isolating it from the supernatant by centrifugation, the pink color precipitate was dried in an oven at 60 °C for 15 min.

2.3. Synthesis of the $Co_3[Co(CN)_6]_2/Fe_3O_4$ Nanocomposite. Ferromagnetic nanoparticles (Fe_3O_4 NPs) were synthesized by following the coprecipitation method reported by Santos et al. with some modifications.[50] Fe_3O_4 NPs were prepared using a 2:1 stoichiometric ratio of $FeCl_3 \cdot 6H_2O$ and $FeCl_2 \cdot 4H_2O$ precursors. In a 25 mL reaction flask, 0.25 mmol (67.57 mg) of $FeCl_3 \cdot 6H_2O$ and 0.125 mmol (24.85 mg) of $FeCl_2 \cdot 4H_2O$ were added. This mixture was left to stir in an ultrasonic bath for 20 min, followed by purging with nitrogen at 25 °C for 5 min. Then, a 1.0 mol L^{-1} NaOH solution was added dropwise to the mixture until the supernatant became colorless. This occurred at pH 10, indicating that all iron ions were consumed with the formation of a black precipitate (Fe_3O_4 NPs). This mixture was maintained at 45 °C for 30 min under magnetic stirring and N_2 atmosphere. The Fe_3O_4 powder was separated from the supernatant with a magnet, washed thrice with acetone until the supernatant reached pH ~6.5, and then dried in an oven at 100 °C for 15 min. The $Co_3[Co(CN)_6]_2/Fe_3O_4$ nanocomposite was prepared using the synthesis strategy described by Melo et al.[51] and Zhao and co-

workers[52] for producing Fe_3O_4–Prussian blue. The Fe_3O_4 NP powder was added to 10 mL of an aqueous solution containing 5×10^{-5} mol of $K_3[Co(CN)_6]$ (16.6 mg). This was followed by the slow dropwise addition of 10 mL of 7.5×10^{-5} mol $Co(CH_3COO)_2 \cdot 4H_2O$ (18.7 mg) to the reaction mixture, which was then stirred for 12 h at 25 °C under an inert atmosphere. Finally, the black colored $Co_3[Co(CN)_6]_2/Fe_3O_4$ product was washed thrice with acetone to remove the nonadsorbed or weakly adsorbed Fe_3O_4 NPs on the $Co_3[Co(CN)_6]_2$ surface, isolated from the supernatant by magnetic separation and dried at 60 °C. Figure 1 illustrates the synthesis process of the nanocomposite performed at room temperature.

2.4. Characterization. Ultraviolet−visible (UV−vis) spectra were recorded with an Allcrom UV-6100S double beam spectrophotometer using a quartz cuvette with 1 cm optical path, in the wavelength range of 190−900 nm. The infrared spectra of samples in KBr pellets were obtained with a PerkinElmer Spectrum 100 FTIR spectrometer in two regions, from 4000 to 1800 cm^{-1} and from 1200 to 400 cm^{-1}. The spectra were normalized with maximum and minimum values corresponding to 1.0 and 0.0, respectively. The TEM images were obtained using the TECNAI 20 instrument operated at an accelerating voltage of 200 kV. A drop of the colloidal suspension of $Co_3[Co(CN)_6]_2$ NCs and $Co_3[Co(CN)_6]_2/Fe_3O_4$ was placed on the carbon-coated copper grid, dried at 25 °C, and analyzed by TEM. The XRD patterns were recorded on a Bruker D8 Advance diffractometer using nickel-filtered Cu Kα radiation at a scan rate of 2 and 1 deg/min for $Co_3[Co(CN)_6]_2$ NCs and Fe_3O_4 NPs, respectively, and 0.02 deg/min for $Co_3[Co(CN)_6]_2/Fe_3O_4$, in the 2θ range of 10−70°.

The morphological characteristics and chemical compositions of the materials were studied by scanning electron microscopy (SEM) using a FEI (QUANTA FEG 250 model) microscope equipped with an energy dispersive X-ray spectrometer (EDS) at an accelerating voltage of 20 kV. For SEM analysis, the materials were dispersed in isopropyl alcohol and a drop of this dispersion placed on the aluminum-coated stub was allowed to dry at room temperature. The specific surface areas and pore volumes were measured by Brunauer−Emmett−Teller (BET) analysis of N_2 absorption/desorption isotherms obtained using a Micromeritics AutoChem II 2920 instrument.

To determine the oxidation states of cobalt and iron, and identify the elements at the surface of the samples, high-resolution XPS measurements were carried out. Spectra were acquired using a Scienta Omicron ESCA + Spectrometer system equipped with an EA 125 hemispherical analyzer and a Xm 1000 monochromated Al Kα X-ray source (1486.7 eV). The X-ray source was used with a power of 280 W and the XPS high resolution spectra were recorded at a constant pass energy of 20 eV with 0.05 eV per step. Data analysis was performed using CasaXPS software (version 2.3.16), where the background in high-resolution spectra were computed using the Shirley method. Charge effects were corrected using the C 1s peak at 284.5 eV of adventitious carbon on the sample surface. The electrochemical properties of the materials were studied using cyclic voltammetry (CV) with an Autolab PGSTAT128N potentiostat/galvanostat coupled to a three-electrode electrochemical cell. The reference electrode was saturated calomel (SCE), platinum served as the auxiliary electrode, while the working electrode was a bare ITO slide (indium tin oxide, R_s = 70−100 Ω, Delta Technologies Ltd., Auburn Hills, MI, USA; area of 0.16 cm^2). For CV analysis, 6.42 mg of each material ($Co_3[Co(CN)_6]_2$ NCs and $Co_3[Co(CN)_6]_2/Fe_3O_4$) were dispersed in 20 mL of NaCl electrolyte (0.1 mol L^{-1}, pH 7.2). Oxygen was removed from the electrochemical cell with nitrogen gas flow for 5 min. The magnetization of the nanomaterials was measured with an EZ9 vibrating sample magnetometer (VSM) with the magnetic field varying between −20 and 20 kOe at room temperature.

3. RESULTS AND DISCUSSION

3.1. Spectroscopic Investigation. The supramolecular assembly of the 3D nanohybrid, $Co_3[Co(CN)_6]_2/Fe_3O_4$, was obtained by first dispersing the magnetic nanoparticles in a

solution containing $[Co(CN)_6]^{3-}$ ions. Upon mixing Co^{2+} and $[Co(CN)_6]^{3-}$ ions in the corresponding $Fe_3O_4/[Co(CN)_6]^{3-}$ stoichiometry ratios, the dispersion turned black. This suggested the formation of a new product. The UV−vis spectra of the hybrid and precursors shown in Figure 2 are
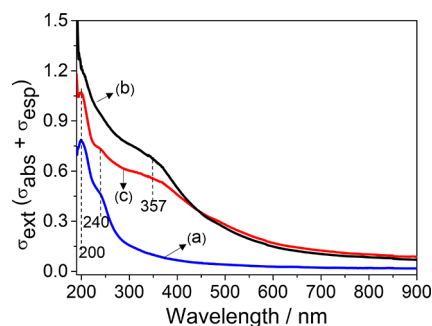
Figure 2. UV−vis spectra for colloidal suspensions of (a) $Co_3[Co(CN)_6]_2$, (b) Fe_3O_4, and (c) $Co_3[Co(CN)_6]_2/Fe_3O_4$.

consistent with the formation of the $Co_3[Co(CN)_6]_2/Fe_3O_4$ hybrid nanomaterial (Figure 2c), whose spectrum was found to be a superposition of the spectra of the starting materials, featuring a band with λ_{max} at 200 nm, a shoulder at 240 nm, and a broad shoulder at 357 nm. For the aqueous dispersion of $Co_3[Co(CN)_6]_2$, the spectrum (Figure 2a) contained an absorption band at 200 nm and a shoulder at 240 nm, thus differing from the spectrum of the cobalt precursors.[39,56] The spectrum of Fe_3O_4 NPs (Figure 2b) had a broad shoulder at 357 nm and was affected by the scattering caused by the nanoparticles.[50,51] Figure S1 shows the spectra for $FeCl_3 \cdot 6H_2O$ and $FeCl_2 \cdot 4H_2O$ solutions, which displayed bands at 291 (ε = 4930 L mol^{-1} cm^{-1}) and 293 nm (ε = 1476 L mol^{-1} cm^{-1}). These bands could be assigned to the metal-to-ligand charge transfer (MLCT) transition in aqua-iron complexes.[53] Figure S1 also shows the spectra of $K_3[Co(CN)_6]$ with two main absorptions at 256 (ε = 208 L mol^{-1} cm^{-1}) and 310 nm (ε = 272 L mol^{-1} cm^{-1}), and $Co(CH_3COO)_2 \cdot 4H_2O_{(aq)}$, which showed a band at 512 nm (ε = 5.6 L mol^{-1} cm^{-1}) assigned to d−d transitions.[39,54,55]

The interactions between $Co_3[Co(CN)_6]_2$ and Fe_3O_4 NPs were investigated by FTIR spectroscopy and the spectra of Fe_3O_4 NPs, $Co_3[Co(CN)_6]_2$, and $Co_3[Co(CN)_6]_2/Fe_3O$ (KBr pellets) are shown in Figure 3. The peaks in the spectra were relatively simple to assign because of the high symmetry of the cobalt complex and the low diversity of atoms in the chemical
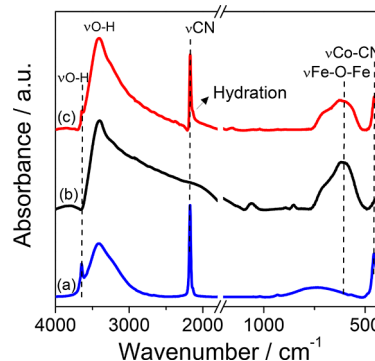
Figure 3. FTIR spectra for (a) $Co_3[Co(CN)_6]_2$ NCs, (b) Fe_3O_4 NPs, and (c) $Co_3[Co(CN)_6]_2/Fe_3O_4$ in KBr pellets.

environment. The broad absorption (high intensity) at 3330–3470 cm^{-1} in Figure 3a was assigned to the stretching mode of H$_2$O (ν(O–H)), which is typical of uncoordinated water.[53,57] In the cases of Co$_3$[Co(CN)$_6$]$_2$ and the hybrid material, the peak at 3646 cm^{-1} was assigned to the stretching mode of water molecules bound to the metallic centers, analogous to the observations by Lejeune and collaborators.[57] The peak at 2135 cm^{-1} (Figure 3a and 3c) is typical of the hydration of the complex analogue, as suggested by Shriver and Brown.[36] The high-intensity band at 2174 cm^{-1} was assigned to ν(C–N) in the Co^{2+}–CN–Co^{3+} fragment for the cobalt complex without and with magnetic nanoparticles. Additional medium intensity bands were observed at 456 ν(Co–CN), and those at 440 and 611 cm^{-1} corresponding to ν(Fe–O) and ν(Fe–O–Fe), respectively, were assigned to the cobalt Prussian blue analogue[39,49] and magnetite.[50–53] Overall, the spectrum of the hybrid material was the superposition of the spectra of the starting materials, Fe$_3$O$_4$ NPs and Co$_3$[Co(CN)$_6$]$_2$. This was confirmed by analyzing the theoretical spectrum of the hybrid material, which was generated from a combination of the experimental FTIR spectra of magnetite and cobalt complex and the experimental spectrum of the hybrid material (Figure S2).

3.2. Crystallinity and Supramolecular Organization.
X-ray diffraction was used to investigate the crystallinity of the nanoparticles and hybrid material. Figures 4a and 4b show the
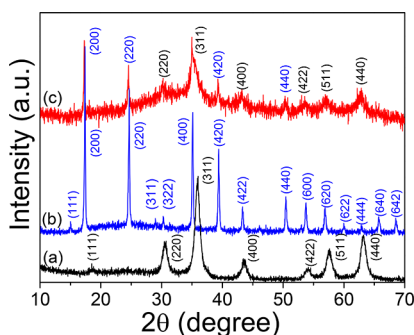

Figure 4. Diffractogram for (a) Fe$_3$O$_4$, (b) Co$_3$[Co(CN)$_6$]$_2$, and (c) Co$_3$[Co(CN)$_6$]$_2$/Fe$_3$O$_4$.

XRD patterns of Fe$_3$O$_4$ and Co$_3$[Co(CN)$_6$]$_2$ samples, which correspond to the inverse cubic spinel structure (JCPDS No. 76-1849) and face-centered cubic (fcc) phase (JCPDS No. 77-1161), respectively. The diffractogram for the Co$_3$[Co-(CN)$_6$]$_2$/Fe$_3$O$_4$ hybrid (Figure 4c) showed peaks from both Co-PBA at 17° (200), 25° (220), 39° (420), and 50° (440), characteristic of the fcc phase, and the inverse Fe$_3$O$_4$ spinel structure at 30° (220), 35° (311), 43° (400), 53° (422), 57° (511), and 63° (440).[35,49,58] The (311) and (200) crystallographic planes had higher intensity peaks owing to the crystalline phase of Fe$_3$O$_4$NPs and Co$_3$[Co(CN)$_6$]$_2$. However, Co$_3$[Co(CN)$_6$]$_2$/Fe$_3$O$_4$ had a less ordered structure than its precursors, as indicated by the broader reflections, similar to other supramolecular structures of magnetite nanoparticles modified with Prussian blue.[59,60] It should be mentioned that the diffractograms in Figure 4a and 4b are those of nanomaterials obtained via synthetic routes designed to investigate diffraction planes and not their relative intensities. Indeed, it is reasonable to expect that the isolated materials are more crystalline than the hybrid material.

The structural organization, shape, and size of the materials were observed by TEM. The TEM images and selected area electron diffraction (SAED) pattern for the isolated Fe$_3$O$_4$ sample are shown in Figure S3, where Fe$_3$O$_4$ nanoparticles were found to be polydisperse, having a quasi-spherical shape with diameter between 5 and 43 nm. Fe$_3$O$_4$ NP aggregates were formed as expected because of their large surface areas and magnetic dipole–dipole interactions.[50]

Well-defined nanocubes, with average edge lengths of 21–140 nm, were formed from the colloidal dispersions of Co$_3$[Co(CN)$_6$]$_2$, as shown in the TEM images (Figure 5a and 5b). There was some contact between the nanocubes in the latter images, which was confirmed in the subsidiary Figure S4a and S4b. In the case of the Co$_3$[Co(CN)$_6$]$_2$/Fe$_3$O$_4$ nanohybrid, Figure 5c and 5d show the spheres and nanocubes corresponding to Fe$_3$O$_4$ NPs and the cobalt Prussian blue analogue, respectively. The Fe$_3$O$_4$ NPs were polydisperse with aggregates smaller than 10 nm in size. The incorporation of these nanoparticles did not affect the size of the 3D Co$_3$[Co(CN)$_6$]$_2$ nanocubes, probably because the magnetite nanoparticles coating the nanocubes prevented them from having contact. The nonuniform distribution of the Fe$_3$O$_4$ NP aggregates on the surface of the nanocubes could be attributed to strong magnetic dipole–dipole interactions[61,62] among the dispersed magnetite nanoparticles during in situ formation of Co$_3$[Co(CN)$_6$]$_2$. This organization was analyzed in more detail in another microregion in Figure 5e, where the Co-PBA nanocubes of ~95 nm size were decorated with 10 nm Fe$_3$O$_4$ aggregates. It is worth noting in Figure 5f that the Co$_3$[Co(CN)$_6$]$_2$ surface was practically entirely coated with the Fe$_3$O$_4$ nanoparticles. A similar supramolecular organization was reported by Chen and co-workers[39] in a catalyst comprising Pd NPs with Co$_3$[Co(CN)$_6$]$_2$, which exhibited a core−shell-like feature with fine Pd particles deposited on the Co$_3$[Co(CN)$_6$]$_2$ nanocubes. The decoration of Co-PBA nanocubes with β-CD led to a decrease in their average length from 115 to 85 nm because the CD layer hampered the growth of the nanocubes.[39] A core−shell structure with Prussian blue and magnetic nanoclusters (PB-MNS) having a hydrodynamic diameter of ~280 nm proved to be effective in the removal of radioactive cesium via magnetic separation of the absorbent from ^{137}Cs-contaminated water.[48]

The crystalline structure of the materials was determined by SAED. Figure S3d shows the (220), (311), (511), and (440) crystallographic planes of Fe$_3$O$_4$, which correspond to the XRD pattern shown in Figure 4a. The SAED pattern for Co$_3$[Co-(CN)$_6$]$_2$ nanocrystal shown in Figure S4d indicated that it was a polycrystalline complex;[63] the crystallographic planes (200), (220), (400), (420), and (422) were consistent with the fcc cobalt PBA structures (Figure 4b). The SAED pattern of the magnetic nanocomposite (Figure S5) had rings related to the (200), (220), and (420) planes of the Co$_3$[Co(CN)$_6$]$_2$ phase and one (311) plane of the Fe$_3$O$_4$ phase. This SAED pattern was consistent with TEM images shown in Figures S5a and 5e, where most of the Co-PBA surface was not decorated by Fe$_3$O$_4$ nanoparticles.

3.3. Surface Properties and Chemical Composition.
The morphology and uniformity of the as-prepared materials were analyzed by SEM at different magnification levels (Figures S6 and S7). Figure S6 shows the nonuniform Co$_3$[Co(CN)$_6$]$_2$ aggregates with quasi-cubic shape and ball-shaped nanoparticles.[37] This organization may be attributed to the absence of surfactants, which generally cause agglomer-
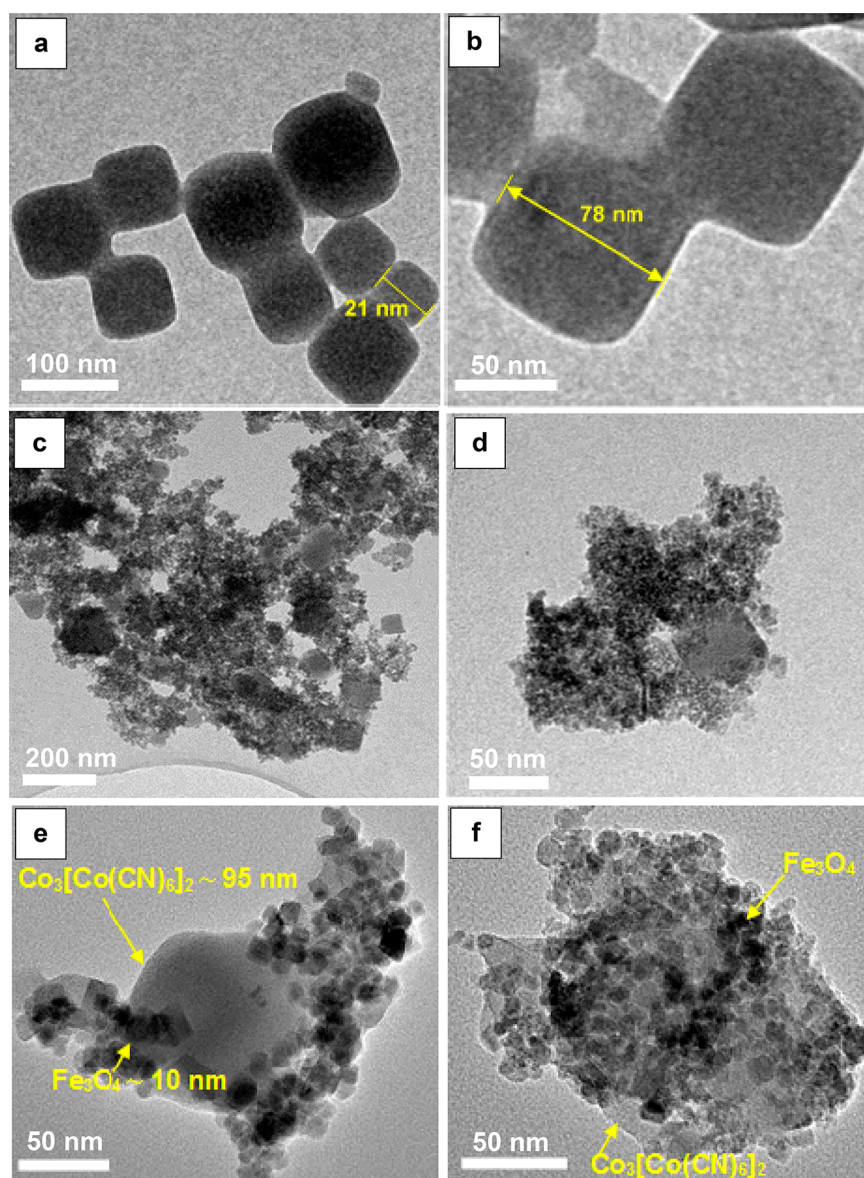
Figure 5. TEM images for $Co_3[Co(CN)_6]_2$, (a) 100 nm (b) 50 nm; $Co_3[Co(CN)_6]_2/Fe_3O_4$, (c) 200 nm, (d) 50 nm, (e) 50 nm, and (f) 50 nm different microregion.

ation to minimize the surface energy. The EDS spectrum of the selected area in Figure S8 reveals the absence of impurities with detection of only C, N, and Co, in addition to Al from the substrate. These results confirm the expected elemental composition of the $Co_3[Co(CN)_6]_2$ complex. The EDS elemental mappings in Figures S8e−S8h also confirmed that the Co-PBA nanocrystals contained C, N, and Co that were well-distributed on the nanocube surfaces. The SEM images of $Co_3[Co(CN)_6]_2/Fe_3O_4$ (Figure S7) illustrate a morphology differing from that of $Co_3[Co(CN)_6]_2$, since these agglomerates were decorated by small particles of varied sizes and spherical or quasi-spherical shape. The EDS analysis (Figure 6h) indicated that the magnetic nanocomposite comprised C, N, O, Fe, and Co, according to the chemical structure of $Co_3[Co(CN)_6]_2/Fe_3O_4$ (Figure S9). Furthermore, it is evident from Figure 6b that $Co_3[Co(CN)_6]_2$ was not fully coated by Fe and O (Fe_3O_4), which corroborates the TEM images. From the EDS elemental mappings in Figure 6c−6g, it could be

noted that the five constituent elements (C, N, O, Fe, and Co) were well-distributed over the sample.

The BET specific surface area and pore volume of Fe_3O_4 nanoparticles were 124.95 m^2 g^{-1} and 0.0629 cm^3 g^{-1}, respectively (Table S1). This surface area is higher than usual for magnetite,[46,64−66] probably because of the synthetic route adopted in this study. The BET areas of $Co_3[Co(CN)_6]_2$ and $Co_3[Co(CN)_6]_2/Fe_3O_4$ were calculated to be 553.13 and 179.01 m^2 g^{-1}, respectively. The pore volume of the Co-PBA nanocubes (0.2785 cm^3 g^{-1}) was higher[67] than that found in $Co_3[Co(CN)_6]_2/Fe_3O_4$ (0.0901 cm^3 g^{-1}), which suggested that the hybrid is a promising material for catalysis. The BET areas were consistent with the TEM images because the specific surface area and pore volume should decrease when decorated by Fe_3O_4 nanoparticles as the Co-PBA surface and pores become occupied. Moreover, the BET area of 179.01 m^2 g^{-1} was also higher than that of magnetite (124.95 m^2 g^{-1}), which indicated that the surface of $Co_3[Co(CN)_6]_2$ was not fully decorated by the Fe_3O_4 nanoparticles.

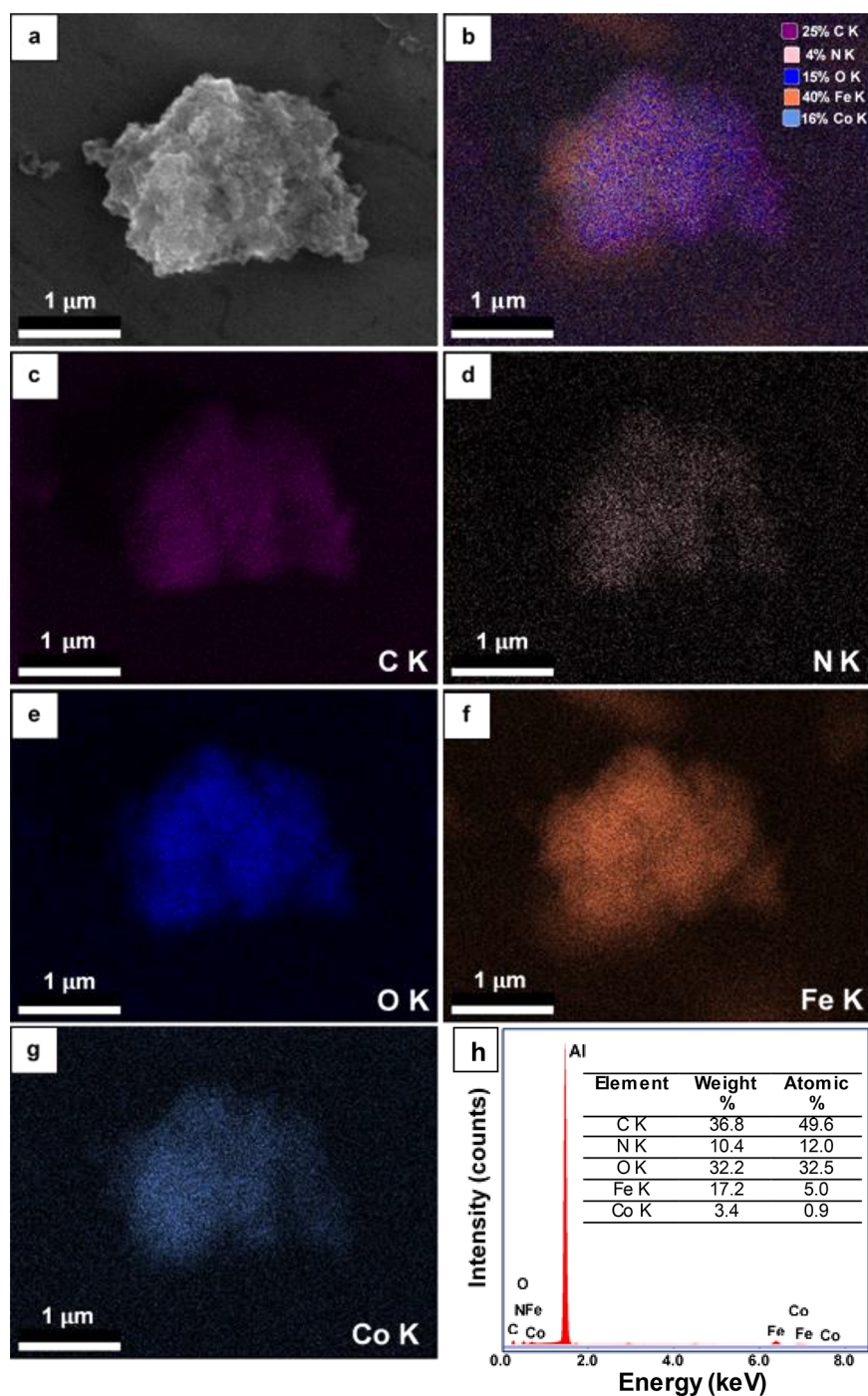**Figure 6.** (a) SEM image of $Co_3[Co(CN)_6]_2/Fe_3O_4$, (b) corresponding EDS elemental mapping of C, N, O, Fe, and Co elements, (c) C mapping, (d) N mapping, (e) O mapping, (f) Fe mapping, (g) Co mapping, and (h) spectrum EDS of aggregates ($Co_3[Co(CN)_6]_2/Fe_3O_4$) microregion.

XPS was used to determine the surface composition in detail, and the full XPS spectra are given in Figure S10. The XPS survey confirmed the presence of Fe, C, O, and Na in the Fe_3O_4 sample, of Co, C, O, and N in the $Co_3[Co(CN)_6]_2$ sample, and of Co, Fe, C, O, and N in the $Co_3[Co(CN)_6]_2/Fe_3O_4$ sample. The presence of Na as an impurity was only detected in Fe_3O_4 because of an excess of NaOH. The surface elemental composition was determined from the survey XPS spectra by calculating the atomic concentration of each element using the specific elemental sensitivity factors, as shown in Table 1.

Table 1. Atomic Percent Concentration of Fe, Co, N, and O Elements (at%) Obtained from XPS Survey Spectra for Fe_3O_4, $Co_3[Co(CN)_6]_2$ and $Co_3[Co(CN)_6]_2/Fe_3O_4$ Samples

sample	Fe 2p (at %)	Co 2p (at %)	N 1s (at %)	O 1s (at %)
Fe_3O_4	18.0			82.0
$Co_3[Co(CN)_6]_2$		14.8	22.6	62.6
$Co_3[Co(CN)_6]_2/Fe_3O_4$	9.0	7.8	20.2	63.1

The deconvolution of the XPS high-resolution spectra of Co 2p in $Co_3[Co(CN)_6]_2$ revealed two spin−orbit doublets

arising from $2p_{3/2}$ and $2p_{1/2}$ at 781.3 and 796.4 eV, respectively. The Co $2p_{3/2}$ component was fitted with two components at 781.1 and 782.4 eV, corresponding to Co^{3+} and Co^{2+}, respectively (Figure 7a).[29,68] The difference in the
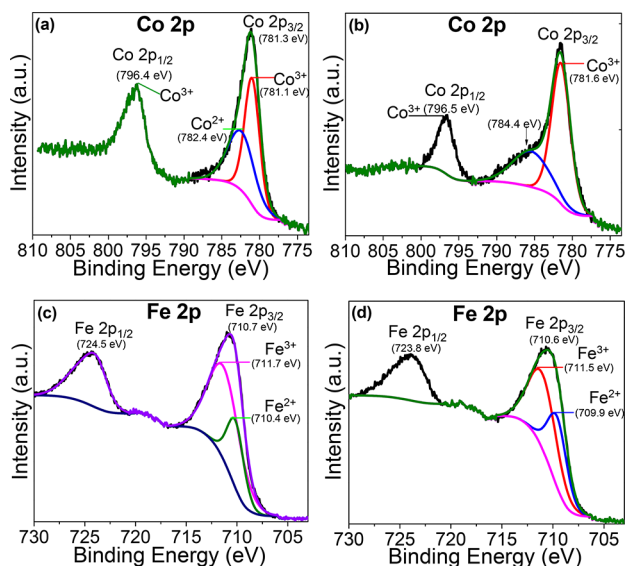

Figure 7. Core-level spectra of Co 2p: (a) $Co_3[Co(CN)_6]_2$ and (b) $Co_3[Co(CN)_6]_2/Fe_3O_4$. Core-level spectra of Fe 2p: (c) Fe_3O_4 and (d) $Co_3[Co(CN)_6]_2/Fe_3O_4$.

binding energy between Co $2p_{3/2}$ and Co $2p_{1/2}$ was 15.1 eV, consistent with the literature reported values.[29] This result confirmed the presence of Co^{2+} and Co^{3+} species, and therefore the formation of $Co_3^{2+}[Co^{3+}(CN)_6]_2$.[68] The high-resolution XPS spectrum of Co 2p in $Co_3[Co(CN)_6]_2/Fe_3O_4$ (Figure 7b) showed a shoulder at ∼784.4 eV, which was absent in $Co_3[Co(CN)_6]_2$. According to previous reports, the appearance of a shoulder at this energy is characteristic of the CoO phase.[69] The peak positions for Fe $2p_{3/2}$ and Fe $2p_{1/2}$ in Fe_3O_4 (Figure 7c) at 710.7 and 724.5 eV, respectively, were in agreement with the literature.[65,66] The Fe 2p peak for Fe_3O_4 was deconvoluted into Fe^{2+} and Fe^{3+} peaks at 710.4 and 711.7 eV, respectively. The presence of both ions confirmed the formation of Fe_3O_4.[65,66] The high-resolution XPS spectrum of Fe 2p in $Co_3[Co(CN)_6]_2/Fe_3O_4$ shown in Figure 7d is quite similar to the Fe 2p core-level spectrum of the Fe_3O_4 sample with deconvoluted peaks assigned to Fe^{2+} at 709.9 eV and to Fe^{3+} at 711.0 eV.

3.4. Electrochemical and Magnetic Properties of Self-Assembled Supramolecular Nanocubes. The electrochemical properties of the 3D hybrid nanomaterial were studied using CV. The voltammogram for the cobalt Prussian blue analogue complex (Figure 8a, blue line) exhibited a redox couple with a formal potential ($E_{1/2}$) of 0.45 V and peak-to-peak separation (ΔE_p) of 0.04 at 0.01 V s^{-1} assigned to the Co^{2+}/Co^{3+} couple. After immobilization of Fe_3O_4 NPs on the $Co_3[Co(CN)_6]_2$ nanocubes, the peak potentials remained practically the same. However, the Faradaic currents increased in comparison with the case of the cobalt Prussian blue analogous species (red line). This suggested that Fe_3O_4 enhanced electron transfer without affecting other electrochemical parameters such as the reversibility and stability of the nanocubes. This increase in current may be related to both the larger amount of electroactive species on the electrode
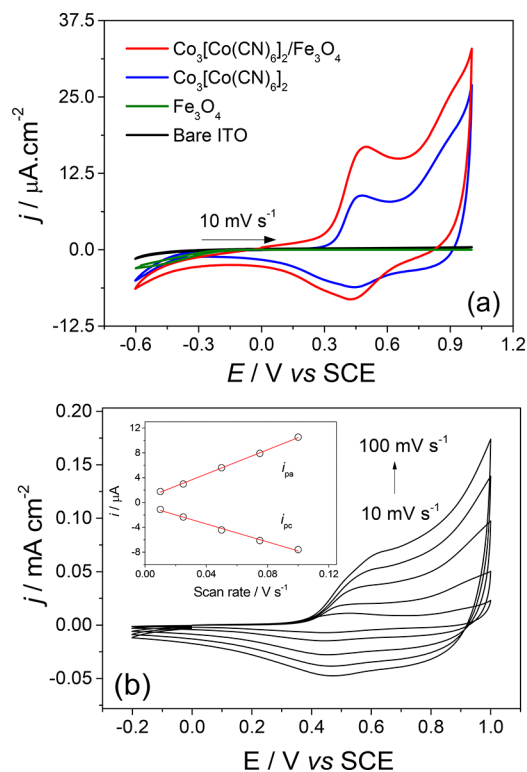

Figure 8. Cyclic voltammograms for (a) $Co_3[Co(CN)_6]_2/Fe_3O_4$ (red line), $Co_3[Co(CN)_6]_2$ (blue line), Fe_3O_4 (green line) and bare ITO (black line) recorded at 0.01 V s^{-1} and (b) CVs recorded at different scan rates for $Co_3[Co(CN)_6]_2/Fe_3O_4$. Inset: Anodic (i_{pa}) and cathodic (i_{pc}) peak currents versus scan rate. Electrolyte: 0.1 mol L^{-1} NaCl, T = 25 °C.

surface and supramolecular charge transfer between the cobalt Prussian blue analogue and the magnetic nanoparticles. The surface coverage (Γ) of $Co_3[Co(CN)_6]_2$ and $Co_3[Co(CN)_6]_2/Fe_3O_4$ on the ITO electrode was estimated based on the integration of CV area according to $\Gamma = Q/nFA$ at 0.01 V s^{-1}, where Q is the charge involved in the electrochemical reaction, n refers to the number of electrons transferred ($n = 1$), F is Faraday's constant, and A is the electrode area (0.16 cm^2). As expected, the surface coverage of $Co_3[Co(CN)_6]_2/Fe_3O_4$ on the ITO electrode ($\Gamma = 1.72 \times 10^{-9}$ mol cm^{-2}) was higher than that of $Co_3[Co(CN)_6]_2$ ($\Gamma = 0.83 \times 10^{-9}$ mol cm^{-2}). Similar behavior was observed for $Co_3[Co(CN)_6]_2$-CD, which contained β-CD on the surface of the 3D nanocubes,[39] and for the layer-by-layer films made with tetrasulfonated nickel phthalocyanine/gold nanoparticles[70] and tetrasulfonated cobalt phthalocyanine/carbon nanotubes.[71] Figure 8b shows that the peak current increased linearly with the scan rate, implying that the electrochemical processes are governed by electron transfer at the cobalt complex/electrode interface, as observed previously for $Co_3[Co(CN)_6]_2$.[39] Although further studies with different electrolytes, ionic forces, and substrates are required to completely understand the electrochemical performance, the $Co_3[Co(CN)_6]_2/Fe_3O_4$ is already being used as an electrochemical sensor for cholesterol detection in our laboratory. Interesting approaches to develop hybrid materials for energy storage devices[72] and supercapacitors,[73] respectively, have been reported in the literature.

Figure 9 shows the hysteresis curves for pure magnetite and the aggregate with the cobalt Prussian blue analogue. Curves of such shape can represent two types of magnetic behavior,
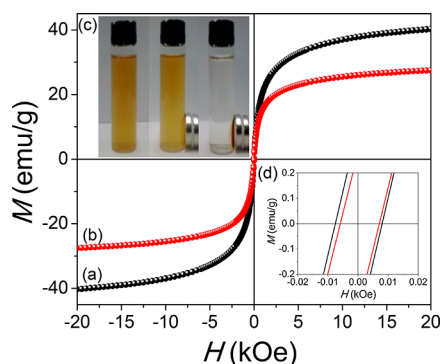
Figure 9. Magnetization as a function of applied magnetic field at room temperature for (a) pure Fe_3O_4 and (b) $Co_3[Co(CN)_6]_2/Fe_3O_4$. Insets: (c) Magnetization effect for the hybrid material and (d) zoomed figure for the magnetization curves.

namely, ferromagnetism (FM) and superparamagnetism (SPM). Saturation is expected to occur rapidly for a ferromagnetic material because the coercive field is practically null (Figure 9, insert d), which does not occur. This analysis led us to believe that the hybrid material showed superparamagnetic behavior (at room temperature), which could be expected from the diameter size that was smaller than 10 nm according to the TEM images (Figure 5). The magnetic properties of the nanoparticles depend on the diameter and temperature of the experiment.[74] SPM is characterized by the reduced remnant and coercive fields, and a nonsaturating behavior for a relatively intense magnetic field, as observed in the magnetic curves in Figure 9d. Mixing the materials did not lead to any significant change in the resulting magnetic response, thus indicating the small influence of the cobalt Prussian blue analogue on the magnetic properties of magnetite. The reduction in M (H = 20 kOe) for $Co_3[Co(CN)_6]_2/Fe_3O_4$ results from the nonmagnetic mass fraction of $Co_3[Co(CN)_6]_2$ used for calculating the emu/g scale. The magnetic behavior of pure $Co_3[Co(CN)_6]_2$ in Figure S11 is typical of paramagnetic response. According to the literature,[61] Prussian blue-coated Fe_3O_4 shows smaller room temperature magnetization (20 emu/g) than neat Fe_3O_4 (45 emu/g) because Prussian blue has virtually no magnetization response to the applied field.

As observed in the FTIR and UV−vis measurements, there were no changes in the electronic transitions and in the stretching bands corresponding to the main functional groups in $Co_3[Co(CN)_6]_2/Fe_3O_4$, thus indicating that the driving force to form the supramolecular structure was probably neither covalent bonding (e.g., metal−ligand) nor reversible noncovalent interactions (e.g., van der Waals and H-bonding). Rather, the self-assembly of Fe_3O_4 NPs aggregates on the nanocubes (Figure 5d) was attributable to the magnetic dipole interactions between the inorganic components at the nanoscale.[59,60,75,76] This conclusion is based on the experimental observation of the small magnetic effect of $Co_3[Co(CN)_6]_2$, whereby it took ~50 min for all the material to be attracted by a magnet (Figure S12). In contrast, under the same conditions, $Co_3[Co(CN)_6]_2/Fe_3O_4$ was magnetically attracted within 10 min. Assemblies in hybrid materials may allow one to achieve synergy in the properties of their constituents, thus leading to advanced functional materials.[77] The formation of a functional hybrid does not occur only by the physical mixing of two materials. Fe_3O_4 NPs exert a strong

influence on the magnetism of $Co_3[Co(CN)_6]_2/Fe_3O_4$ (Figure S12), and the physical adsorption between the materials forming the nanohybrid is driven by the magnetic property.

4. CONCLUSIONS

On the basis of the concept of self-assembly, a nanomaterial composite of the cobalt Prussian blue analogue and magnetite nanoparticles was synthesized. The 3D hybrid nanomaterial exhibited a nanocubic shape decorated with small, spherical magnetite NPs that interacted via dipole−dipole interactions and prevented intimate contact between the nanocubes. The UV−vis spectrum of $Co_3[Co(CN)_6]_2/Fe_3O_4$ colloidal dispersion showed an increase in the baseline owing to light scattering according to the Mie theory. The hybrid nanomaterial showed a well-defined Co^{2+}/Co^{3+} couple in the CV and increased faradaic currents as compared to isolated $Co_3[Co(CN)_6]_2$. The $Co_3[Co(CN)_6]_2/Fe_3O_4$ nanocomposite had a magnetic response similar to that of magnetite nanoparticles. Furthermore, the nanocomposite has promising catalytic activity, which can be combined with its magnetic properties. Therefore, the approach presented here is an avenue for producing hybrid materials with combined electrochemical and magnetic properties.

ASSOCIATED CONTENT

Ⓢ Supporting Information

The Supporting Information is available free of charge on the ACS Publications website at DOI: 10.1021/acsanm.8b01106.

Electronic spectra in the UV−vis region for solution of 0.2×10^{-3} mol L^{-1} $FeCl_3 \cdot 6H_2O$, 0.6×10^{-3} mol L^{-1} $FeCl_2 \cdot 4H_2O$, 3×10^{-3} mol L^{-1} $K_3[Co(CN)_6]$, and 0.1 mol L^{-1} $Co(CH_3COO)_2 \cdot 4H_2O$; FTIR spectra for experimental spectrum hybrid material and theoretical spectrum of the mixture (generated from the combination of experimental spectra FTIR of $Co_3[Co(CN)_6]_2$ and da Fe_3O_4); TEM images for Fe_3O_4, $Co_3[Co(CN)_6]_2$, and $Co_3[Co(CN)_6]_2/Fe_3O_4$; SEM images for $Co_3[Co(CN)_6]_2$, $Co_3[Co(CN)_6]_2/Fe_3O_4$, and $Co_3[Co(CN)_6]_2$; corresponding EDS analysis of unallocated microregion and aggregate ($Co_3[Co(CN)_6]_2$) microregion, spectrum EDS of unallocated and aggregate microregion, corresponding EDS elemental mappings for C, N, and Co elements; SEM of $Co_3[Co(CN)_6]_2/Fe_3O_4$ and corresponding EDS spectrum; BET specific surface areas and pore volumes of Fe_3O_4, $Co_3[Co(CN)_6]_2$, and $Co_3[Co(CN)_6]_2/Fe_3O_4$; full-survey XPS spectrum for Fe_3O_4, $Co_3[Co(CN)_6]_2$, and $Co_3[Co(CN)_6]_2/Fe_3O_4$; magnetization measurements as a function of applied magnetic field for $Co_3[Co(CN)_6]_2$ NCs; and schematic representation of the magnetism of $Co_3[C_O(CN)_6]_2$ and $Co_3[Co(CN)_6]_2/Fe_3O_4$ (PDF)

AUTHOR INFORMATION

Corresponding Authors

*E-mail: welter@ufpi.edu.br. Tel.: +55-86-3215-5840. Fax: +55-86-3215-5692.

*E-mail: chu@ifsc.usp.br. Tel. + 55-16-3373-9825.

ORCID

Caio Lenon C. Carvalho: 0000-0001-7133-054X

Anna Thaise B. Silva: 0000-0001-8921-8804

Roberto A. S. Luz: 0000-0003-0045-6959

Gustavo Montgomery B. Castro: 0000-0002-1897-3877
Cleanio da Luz Lima: 0000-0003-3958-7008
Valmor Roberto Mastelaro: 0000-0001-9512-4214
Robson Rosa da Silva: 0000-0001-6887-4749
Osvaldo N. Oliveira, Jr.: 0000-0002-5399-5860
Welter Cantanhêde: 0000-0003-4673-9604

Notes

The authors declare no competing financial interest.

◼ REFERENCES

(1) Hazut, O.; Waichman, S.; Subramani, T.; Sarkar, D.; Dash, S.; Roncal-Herrero, T.; Kroger, R.; Yerushalmi, R. Semiconductor−Metal Nanofloret Hybrid Structures by Self Processing Synthesis. *J. Am. Chem. Soc.* **2016**, *138*, 4079−4086.

(2) Goldmann, C.; Lazzari, R.; Paquez, X.; Boissière, C.; Ribot, F.; Sanchez, C.; Chanéac, C.; Portehault, D. Charge Transfer at Hybrid Interfaces: Plasmonics of Aromatic Thiol-Capped Gold Nanoparticles. *ACS Nano* **2015**, *9*, 7572−7582.

(3) Pandey, P. C.; Prakash, A.; Pandey, A. K. Studies on Electrochemical and Peroxidase Mimetic Behavior of Prussian Blue Nanoparticles in Presence of Pd-WO3-SiO2 Nanocomposite; Bioelectro-Catalytic Sensing H2O2. *Electrochim. Acta* **2014**, *127*, 132−138.

(4) Banin, U.; Ben-Shahar, Y.; Vinokurov, K. Hybrid Semiconductor−Metal Nanoparticles: From Architecture to Function. *Chem. Mater.* **2014**, *26*, 97−110.

(5) Lou, L.; Yu, K.; Zhang, Z.; Huang, R.; Wang, Y.; Zhu, Z. Facile Methods for Synthesis of Core-Shell Structured and Heterostructured Fe3O4@Au Nanocomposites. *Appl. Surf. Sci.* **2012**, *258*, 8521−8526.

(6) Wei, P.; Yan, X.; Huang, H. Supramolecular Polymers Constructed by Orthogonal Self-Assembly Based on Host−Guest and Metal−Ligand Interactions. *Chem. Soc. Rev.* **2015**, *44*, 815−832.

(7) Nonkumwong, J.; Pakawanit, P.; Wipatanawin, A.; Jantaratana, P.; Ananta, S.; Srisombat, L. Synthesis and Cytotoxicity Study of Magnesium Ferrite-Gold Core-Shell Nanoparticles. *Mater. Sci. Eng., C* **2016**, *61*, 123−132.

(8) Zheng, Y.; Yuan, Y.; Chai, Y.; Yuan, R. L-cysteine Induced Manganese Porphyrin Electrocatalytic Amplification With 3D DNA-Au@Pt Nanoparticles as Nanocarriers for Sensitive Electrochemical Aptasensor. *Biosens. Bioelectron.* **2016**, *79*, 86−91.

(9) Chen, J.; Zhu, Y.; Zhang, Y. Glutathione-Capped Mn-doped ZnS Quantum Dots as a Room-Temperature Phosphorescence Sensor for the Detection of Pb2+ ions. *Spectrochim. Acta, Part A* **2016**, *164*, 98−102.

(10) Ou, J.; Zhu, Y.; Kong, Y.; Ma, J. Graphene Quantum Dots/β-Cyclodextrin Nanocomposites: A Novel Electrochemical Chiral Interface for Tryptophan Isomer Recognition. *Electrochem. Commun.* **2015**, *60*, 60−63.

(11) Fragal, H. V.; Cellet, S. P. T.; Pereira, G. M.; Fragal, E. H.; Costa, M. A.; Nakamura, C. V.; Asefa, T.; Rubira, A. F.; Silva, R. Covalently-Layers of PVA and PAA and In Situ Formed Ag Nanoparticles as Versatile Antimicrobial Surfaces. *Int. J. Biol. Macromol.* **2016**, *91*, 329−337.

(12) Sathiyabama, M.; Parthasarathy, R. Biological Preparation of Chitosan Nanoparticles and its In Vitro Antifungal Efficacy Against Some Phytopathogenic Fungi. *Carbohydr. Polym.* **2016**, *151*, 321−325.

(13) Liu, S.; Fu, J.; Wang, M.; Yan, Y.; Xin, Q.; Cai, L.; Xu, Q. Magnetically Separable and Recyclable Fe3O4-Polydopamine Hybrid Hollow Microsphere for Highly Efficient Peroxidase Mimetic Catalysts. *J. Colloid Interface Sci.* **2016**, *469*, 69−77.

(14) Bouilly, D.; Janssen, J. L.; Cabana, J.; Côté, M.; Martel, R. Graft-Induced Midgap States in Functionalized Carbon Nanotubes. *ACS Nano* **2015**, *9*, 2626−2634.

(15) Song, Y.; He, J.; Wu, H.; Li, X.; Yu, J.; Zhang, Y.; Wang, L. Preparation of Porous Hollow CoOx Nanocubes via Chemical Etching Prussian blue Analogue for Glucose Sensing. *Electrochim. Acta* **2015**, *182*, 165−172.

(16) Tanaka, A.; Hashimoto, K.; Kominami, H. Visible-Light-Induced Hydrogen and Oxygen Formation Over Pt/Au/WO3 Photocatalyst Utilizing Two Types of Photoabsorption Due to Surface Plasmon Resonance and Band-Gap Excitation. *J. Am. Chem. Soc.* **2014**, *136*, 586−589.

(17) Tian, X.; Dong, Z.; Hou, J.; Wang, R.; Ma, J. A Fuorescent Sensor base on Magnetic Silica Nanoparticles for Cu2+ and Pyrophosphate Mimicking IMPLICATION Logic Gate. *J. Lumin.* **2014**, *145*, 459−465.

(18) Kim, S.; Lee, J.; Jang, S.; Lee, H.; Sung, D.; Chang, J.-H. High Efficient Chromogenic Catalysis of Tetramethylbenzidine with Horseradish Peroxidase Immobilized Magnetic Nanoparticles. *Biochem. Eng. J.* **2016**, *105*, 406−411.

(19) Shokouhimehr, M.; Soehnlen, E. S.; Hao, J.; Griswold, M.; Flask, C.; Fan, X.; Basilion, J. P.; Basu, S.; Huang, S. D. Dual Purpose Prussian blue Nanoparticles for Cellular Imaging and Drug Delivery: A New Generation of T1-Weighted MRI Contrast and Small molecule Delivery Agents. *J. Mater. Chem.* **2010**, *20*, 5251−5259.

(20) Zhou, S.; Wang, Y.; Zhu, J.-J. Simultaneous Detection of Tumor cell Apoptosis Regulators Bcl-2 and Bax Through a Dual-Signal-Marked Electrochemical Immunosensor. *ACS Appl. Mater. Interfaces* **2016**, *8*, 7674−7682.

(21) Hu, L.; Mei, J.-Y.; Chen, Q.-W.; Zhang, P.; Yan, N. Magnetically Separable Prussian Blue Analogue Mn3[Co(CN)6]2·nH2O Porous Nanocubes as Excellent Absorbents for Heavy Metal Ions. *Nanoscale* **2011**, *3*, 4270−4274.

(22) Rohilla, S.; Aghamkar, P.; Sunder, S.; Kumar, A.; Lal, B. Synthesis and Characterization of Fe4[Co(CN)6]3.16H2O/SiO2 Nano-Composites by Coprecipitation Method. *Adv. Mater. Lett.* **2013**, *4*, 53−57.

(23) Behera, J. N.; D'Alessandro, D. M.; Soheilnia, N.; Long, J. R. Synthesis and Characterization of Ruthenium and Iron-Ruthenium Prussian Blue Analogues. *Chem. Mater.* **2009**, *21*, 1922−1926.

(24) Liu, H.; long Du, X.; Gao, P.; Zhao, J. H.; Fang, J.; Shen, W. Distinct Magnetic Properties of one Novel Type of Nanoscale Cobalt−Iron Prussian Blue Analogues Synthesized in Microemulsion. *J. Magn. Magn. Mater.* **2010**, *322*, 572−577.

(25) Fernandez, C. A.; Nune, S. K.; Motkuri, R. K.; Thallapally, P. K.; Wang, C.; Liu, J.; Exarhos, J. G.; McGrail, B. P. Synthesis, Characterization, and Application of Metal Organic Framework Nanostructures. *Langmuir* **2010**, *26*, 18591−18594.

(26) Bhatt, P.; Banerjee, S.; Anwar, S.; Mukadam, M. D.; Meena, S. S.; Yusuf, S. M. Core−shell Prussian Blue Analogue Molecular Magnet Mn1.5[Cr(CN)6]·mH2O@Ni1.5[Cr(CN)6]·nH2O for hydrogen storage. *ACS Appl. Mater. Interfaces* **2014**, *6*, 17579−17588.

(27) Zhao, Q.; Zhao, M.; Qiu, J.; Pang, H.; Lai, W.-Y.; Huang, W. Facile Synthesis of Mn3[Co(CN)6]2·nH2O Nanocrystals for High-Performance Electrochemical Energy Storage Devices. *Inorg. Chem. Front.* **2017**, *4*, 442−449.

(28) Tokoro, H.; Ohkoshi, S.-I. Novel Magnetic Functionalities of Prussian Blue Analogs. *Dalton Trans.* **2011**, *40*, 6825−6833.

(29) Zhang, H.; Li, C.; Chen, D.; Zhao, J.; Jiao, X.; Xia, Y. Facile Preparation of Prussian Blue Analogue Co3[Co(CN)6]2 with Fine-Tuning Color Transition Temperature as Thermochromic Material. *CrystEngComm* **2017**, *19*, 2057−2064.

(30) Buchold, D. M. H.; Feldmann, C. Synthesis of Nanoscale Co3[Co(CN)6]2 in Reverse Microemulsions. *Chem. Mater.* **2007**, *19*, 3376−3380.

(31) Wang, X.; Zou, L.; Fu, H.; Xiong, Y.; Tao, Z.; Zheng, J.; Li, X. Noble metal free oxygen reduction reaction catalysts derived from

Prussian blue nanocrystals dispersed in polyaniline. *ACS Appl. Mater. Interfaces* **2016**, *8*, 8436−8444.

(32) Yan, L.; Liu, Y.; Zha, K.; Li, H.; Shi, L.; Zhang, D. Scale-Activity Relationship of MnOx-FeOy Nanocage Catalysts Derived from Prussian Blue Analogues for Low-temperature NO Reduction: Experimental and DFT Studies. *ACS Appl. Mater. Interfaces* **2017**, *9*, 2581−2593.

(33) Zheng, S.; Xue, H.; Pang, H. Supercapacitors based on metal coordination materials. *Coord. Chem. Rev.* **2017**, DOI: 10.1016/j.ccr.2017.07.002.

(34) Xu, Y.; Zheng, S.; Tang, H.; Guo, X.; Xue, H.; Pang, H. Prussian blue and its derivatives as electrode materials for electrochemical energy storage. *Energy Storage Materials* **2017**, *9*, 11−30.

(35) Cao, M.; Wu, X.; He, X.; Hu, C. Shape-Controlled Synthesis of Prussian Blue Analogue $Co_3[Co(CN)_6]_2$ Nanocrystals. *Chem. Commun.* **2005**, *17*, 2241−2243.

(36) Shriver, D. F.; Brown, D. B. The Environment of Interstitial Ions in a Prussian Blue Analog, $Co_3[Co(CN)_6]_2$. *Inorg. Chem.* **1969**, *8*, 42−46.

(37) Tang, H.-Y.; Chu, Z.; Li, C.-P.; Ren, X.-M.; Xue, C.; Jin, W. Compact Film Fabrication of Porous Coordination Polymer $Co_3[Co(CN)_6]_2$ and its Reversible Vapochromic Behavior. *Dalton Trans.* **2016**, *45*, 10249−10255.

(38) Li, R.; Li, R.; Wang, C.; Gao, L.; Chen, Q. $Pd-Co_3[Co(CN)_6]_2$ Hybrid Nanoparticles: Preparation, Characterization, and Challenge for the Suzuki−Miyaura Coupling of Aryl Chlorides Under Mild Conditions. *Dalton Trans.* **2016**, *45*, 539−544.

(39) Carvalho, C. L. C.; Silva, A. T. B.; Macedo, L. J. A.; Luz, R. A. S.; Neto, J. M. M.; Filho, U. P. R.; Cantanhêde, W. New Hybrid Nanomaterial Based on Self-Assembly of Cyclodextrins and Cobalt Prussian Blue Analogue Nanocubes. *Int. J. Mol. Sci.* **2015**, *16*, 14594−14607.

(40) Jia, H.; Huang, F.; Gao, Z.; Zhong, C.; Zhou, H.; Jiang, M.; Wei, P. Immobilization of ω-Transaminase by Magnetic $PVA-Fe_3O_4$ Nanoparticles. Biotechnology. *Reports* **2016**, *10*, 49−55.

(41) Ho, C.-H.; Tsai, C.-P.; Chung, C.-C.; Tsai, C.-Y.; Chen, F. R.; Lin, H.-J.; Lai, C.-H. Shape-Controlled Growth and Shape-Dependent Cation Site Occupancy of Monodisperse Fe_3O_4 Nanoparticles. *Chem. Mater.* **2011**, *23*, 1753−1760.

(42) Wu, W.; He, Q.; Jiang, C. Magnetic Iron Oxide Nanoparticles: Synthesis and Surface Functionalization Strategies. *Nanoscale Res. Lett.* **2008**, *3*, 397−415.

(43) Xu, C.; Wang, B.; Sun, S. Dumbbell-Like $Au-Fe_3O_4$ Nanoparticles for Target-Specific Platin Delivery. *J. Am. Chem. Soc.* **2009**, *131*, 4216−4217.

(44) Dong, A.; Lan, S.; Huang, J.; Wang, T.; Zhao, T.; Xiao, L.; Wang, W.; Zheng, X.; Liu, F.; Gao, G.; Chen, Y. Modifying Fe_3O_4-Functionalized Nanoparticles with n-Halamine and Their Magnetic/Antibacterial Properties. *ACS Appl. Mater. Interfaces* **2011**, *3*, 4228−4235.

(45) Sun, X.; Guo, S.; Liu, Y.; Sun, S. Dumbbell-Like $PtPd-Fe_3O_4$ Nanoparticles for Enhanced Electrochemical Detection of H_2O_2. *Nano Lett.* **2012**, *12*, 4859−4863.

(46) Venkateswarlu, S.; Yoon, M. Core−shell Ferromagnetic Nanorod Based on Amine Polymer Composite (Fe_3O_4@DAPF) for Fast Removal of Pb(II) From Aqueous Solutions. *ACS Appl. Mater. Interfaces* **2015**, *7*, 25362−25372.

(47) Ríos, A.; Zougagh, M. Recent Advances in Magnetic Nanomaterials for Improving Analytical Processes. *TrAC, Trends Anal. Chem.* **2016**, *84*, 72−83.

(48) Yang, H.-M.; Jang, S.-C.; Hong, S.-B.; Lee, K.-W.; Roh, C.; Huh, Y. S.; Seo, B.-K. Prussian Blue-Functionalized Magnetic Nanoclusters for the Removal of Radioactive Cesium from Water. *J. Alloys Compd.* **2016**, *657*, 387−393.

(49) Hu, L.; Zhang, P.; Chen, Q.-W.; Mei, J.-Y.; Yan, N. Room-Temperature Synthesis of Prussian Blue Analogue $Co_3[Co(CN)_6]_2$ Porous Nanostructures and their CO_2 Storage Properties. *RSC Adv.* **2011**, *1*, 1574−1578.

(50) Santos, A. F. M.; Macedo, L. J. A.; Chaves, M. H.; Espinoza-Castañeda, M.; Merkoçi, A.; Lima, F. C. A.; Cantanhêde, W. Hybrid Self-Assembled Materials Constituted by Ferromagnetic Nanoparticles and Tannic Acid: A Theoretical and Experimental Investigation. *J. Braz. Chem. Soc.* **2016**, *27*, 727−734.

(51) Melo, A. F. A. A.; Carvalho, V. A. N.; Pagnoncelli, K. C.; Crespilho, F. N. Single Microparticle Applied in Magnetic-Switchable Electrochemistry. *Electrochem. Commun.* **2013**, *30*, 79−82.

(52) Zhao, G.; Feng, J.-J.; Zhang, Q.-L.; Li, S.-P.; Chen, H.-Y. Synthesis and Characterization of Prussian Blue Modified Magnetite Nanoparticles and its Application to the Electrocatalytic Reduction of H_2O_2. *Chem. Mater.* **2005**, *17*, 3154−3159.

(53) Melo, A. F. A. A.; Luz, R. A. S.; Iost, R. M.; Nantes, I. L.; Crespilho, F. N. Highly Stable Magnetite Modified with Chitosan, Ferrocene and Enzyme for Application in Magneto-Switchable Bioelectrocatalysis. *J. Braz. Chem. Soc.* **2013**, *24*, 285−294.

(54) Bitmez, S.; Sayin, K.; Avar, B.; Köse, M.; Kayraldiz, A.; Kurtoglu, M. Preparation, Spectral, X-ray Powder Diffraction and Computational Studies and Genotoxic Properties of New Azo−Azomethine Metal Chelates. *J. Mol. Struct.* **2014**, *1076*, 213−226.

(55) Miskowski, V. M.; Gray, H. B.; Wilson, R. B.; Solomon, E. I. Position of the $^3T_{1g} \leftarrow {}^1A_{1g}$ Transition in Hexacyanocobaltate (III) Analysis of Absorption and Emission Results. *Inorg. Chem.* **1979**, *18*, 1410−1412.

(56) Pyrasch, M.; Toutianoush, A.; Jin, W.; Schnepf, J.; Tieke, B. Self-Assembled Films of Prussian Blue and Analogues: Optical and Electrochemical Properties and Application as Ion-Sieving Membranes. *Chem. Mater.* **2003**, *15*, 245−254.

(57) Lejeune, J.; Brubach, J.-B.; Roy, P.; Bleuzen, A. Application of the Infrared Spectroscopy to the Structural Study of Prussian Blue Analogues. *C. R. Chim.* **2014**, *17*, 534−540.

(58) Adams, S. A.; Hauser, J. L.; Allen, A. C.; Lindquist, K. P.; Ramirez, A. P.; Oliver, S.; Zhang, J. Z. Fe_3O_4@SiO_2 Nanoparticles Functionalized with Gold and Poly(vinylpyrrolidone) for Bio-Separation and Sensing Applications. *ACS Appl. Nano Mater.* **2018**, *1*, 1406−1412.

(59) Kredentser, S. V.; Kulyk, M. M.; Kalita, V. M.; Slyusarenko, K. Y.; Reshetnyak, V. Y.; Reznikov, Y. A. Magneto-Induced Anisotropy in Magnetic Colloids of Superparamagnetic Magnetite Nanoparticles in an External Magnetic Field. *Soft Matter* **2017**, *13*, 4080−4087.

(60) Heinrich, D.; Goñi, A. R.; Osán, T. M.; Cerioni, L. M. C.; Smessaert, A.; Klapp, S. H. L.; Faraudo, J.; Pusiol, D. J.; Thomsen, C. Effects of Magnetic Field Gradients on the Aggregation Dynamics of Colloidal Magnetic Nanoparticles. *Soft Matter* **2015**, *11*, 7606−7616.

(61) Thammawong, C.; Opaprakasit, P.; Tangboriboonrat, P.; Sreearunothai, P. Prussian Blue-Coated Magnetic Nanoparticles for Removal of Cesium From Contaminated Environment. *J. Nanopart. Res.* **2013**, *15*, 1689.

(62) Yang, H.; Sun, L.; Zhai, J.; Li, H.; Zhao, Y.; Yu, H. *In situ* Controllable Synthesis of Magnetic Prussian Blue/Graphene Oxide Nanocomposites for Removal of Radioactive Cesium in Water. *J. Mater. Chem. A* **2014**, *2*, 326−332.

(63) Nie, P.; Shen, L.; Luo, H.; Ding, B.; Xu, G.; Wang, J.; Zhang, X. Prussian blue analogues: a new class of anode materials for lithium ion batteries. *J. Mater. Chem. A* **2014**, *2*, 5852−5857.

(64) Meng, X.; Xu, Y.; Sun, X.; Wang, J.; Xiong, L.; Du, X.; Mao, S. Graphene Oxide Sheets-Induced Growth of Nanostructured Fe_3O_4 for High-performance Anode Material of Lithium Ion Batteries. *J. Mater. Chem. A* **2015**, *3*, 12938−12946.

(65) Zhu, M.; Diao, G. Synthesis of Porous Fe_3O_4 Nanospheres and Its Application for the Catalytic Degradation of Xylenol Orange. *J. Phys. Chem. C* **2011**, *115*, 18923−18934.

(66) Jain, S.; Shah, J.; Dhakate, S. R.; Gupta, G.; Sharma, C.; Kotnala, R. K. Environment-Friendly Mesoporous Magnetite Nanoparticles-Based Hydroelectric Cell. *J. Phys. Chem. C* **2018**, *122*, 5908−5916.

(67) Gao, L.; Wang, C.; Li, R.; Li, R.; Chen, Q. The Effect of External Magnetic Fields on the Catalytic Activity of Pd Nanoparticles in Suzuki Cross-Coupling Reactions. *Nanoscale* **2016**, *8*, 8355−8362.

(68) Lin, A. K-Y.; Lai, H.-K.; Tong, S. One-step prepared cobalt-based nanosheet as an efficient heterogeneous catalyst for activating peroxymonosulfate to degrade caffeine in water. *J. Colloid Interface Sci.* **2018**, *514*, 272−280.

(69) Yang, H.; Ouyang, J.; Tang, A. Single Step Synthesis of High-Purity CoO Nanocrystals. *J. Phys. Chem. B* **2007**, *111*, 8006−8013.

(70) Alencar, W. S.; Crespilho, F. N.; Martins, M. V. A.; Zucolotto, V.; Oliveira, O. N., Jr.; Silva, W. C. Synergistic Interaction Between Gold Nanoparticles and Nickel Phthalocyanine in Layer-by-Layer (LbL) Films: Evidence of Constitutional Dynamic Chemistry (CDC). *Phys. Chem. Chem. Phys.* **2009**, *11*, 5086−5091.

(71) de Sousa Luz, R. A.; Martins, M. V. A.; Magalhães, J. L.; Siqueira, J. R., Jr.; Zucolotto, V.; Oliveira, O. N., Jr.; Crespilho, F. N.; da Silva, W. C. Supramolecular Architectures in Layer-by-Layer Films of Single-Walled Carbon Nanotubes, Chitosan and Cobalt (II) Phthalocyanine. *Mater. Chem. Phys.* **2011**, *130*, 1072−1077.

(72) Pang, H.; Li, B.; Zhao, Q.; Lai, W. Y.; Huang, W. Cu superstructures hydrothermally reduced by leaves and derived Cu−Co_3O_4 hybrids for flexible solid-state electrochemical energy storage devices. *J. Mater. Chem. A* **2016**, *4*, 4840−4847.

(73) Pang, H.; Li, X.; Zhao, Q.; Xue, H.; Lai, W. Y.; Hu, Z.; Huang, W. One-pot synthesis of heterogeneous Co_3O_4-nanocube/$Co(OH)_2$-nanosheet hybrids for high-performance flexible asymmetric all-solid-state supercapacitors. *Nano Energy* **2017**, *35*, 138−145.

(74) Zhang, Q.; Jiang, Z.; Yan, B. Ultrasmall and Monodisperse Colloidal Amorphous Nd−Fe−B−Na Magnetic Nanoparticles with High. *Inorg. Chem. Front.* **2014**, *1*, 384−388.

(75) Bishop, K. J. M.; Wilmer, C. E.; Soh, S.; Grzybowski, B. A. Nanoscale Forces and Their Uses in Self-Assembly. *Small* **2009**, *5*, 1600−1630.

(76) Min, Y.; Akbulut, M.; Kristiansen, K.; Golan, Y.; Israelachvili, J. The Role of Interparticle and External Forces in Nanoparticle Assembly. *Nat. Mater.* **2008**, *7*, 527−538.

(77) Stupp, S. I.; Palmer, L. C. Supramolecular Chemistry and Self-Assembly in Organic Materials Design. *Chem. Mater.* **2014**, *26*, 507−518.